Revision2

High-temperature structural change and microtexture formation of sillimanite and its phase relation with mullite

Yohei Igami[1, 2*], Shugo Ohi[3], Tetsu Kogiso[4], Noboru Furukawa[5], and Akira Miyake[1]

[1] Graduate School of Science, Kyoto University, Kyoto 606-8502, Japan

[2] Institute of Materials and Systems for Sustainability, Nagoya University, Nagoya 464-8603, Japan

[3] Faculty of Education, Shiga University, Ohtsu 520-0862, Japan

[4] Graduate School of Human and Environmental Studies, Kyoto University, Kyoto 606-8501, Japan

[5] Graduate School of Science, Chiba University, Chiba 263-8522, Japan

[*]Corresponding author. E-mail: y-igami@nagoya-u.jp

Abstract

Synchrotron powder X-ray diffraction (XRD) experiments and transmission electron microscopy (TEM) observations of heat-treated sillimanite at various pressures were conducted to clarify the detailed phase relation between sillimanite and mullite. Under TEM, heat-treated sillimanite frequently showed anti-phase boundary (APB)-like textures

with a displacement vector of $1/2[001]_{sil}$. Additional scanning TEM-energy dispersive X-ray spectroscopy analysis of regions with APB-like texture showed that they were clearly enriched in Al and accompanied by very fine, Si-rich glass inclusions, which indicates that the APB-like textures are composed of fine mullite. Moreover, synchrotron XRD patterns of these samples clearly showed double peaks of newly formed mullite and remnant sillimanite, indicating that the compositional transformation from sillimanite to mullite and glass is discontinuous. We separately determined the cell parameters of the sillimanite and mullite from the XRD pattern and found that the *b* axial length of the sillimanite increased with the treatment temperature, reflecting disordering of tetrahedral Al and Si in the sillimanite. In contrast, the positions of the deconvoluted mullite peaks indicated that the *a* axial length of mullite decreased as experimental pressure increased, owing to enrichment of the Si component. By projecting the cell parameters onto the *a*–*b* axial plane, the detailed changes in the crystallographic state of the sillimanite and mullite could be easily and comprehensively identified. On the basis of our results, we propose a new *P*–*T* diagram for the Al_2SiO_5 system that shows the transformation boundary between sillimanite and mullite + SiO_2-rich melt and the contour of the Al/Si order parameter of sillimanite.

Keywords: sillimanite, mullite, high-temperature phase relation, TEM observation, synchrotron X-ray experiment

Introduction

Naturally occurring polymorphs of Al_2SiO_5 (andalusite, kyanite, sillimanite) have assumed a special significance for geologists because of their abundance in metamorphic rocks and their simple pressure–temperature (*P*–*T*) phase relations. Although the phase relations in this system have been investigated over many years, however, some problems persist, in particular, related to sillimanite.

The crystal structure of sillimanite [space group *Pbnm* (No. 62)] is characterized by chains of edge-sharing AlO_6 octahedra (AlO_4 octahedral chains) linked to double SiO_4/AlO_4 tetrahedral chains parallel to the *c*-axis, with the SiO_4 and AlO_4 tetrahedra arranged alternately. Zen (1969) considered that disordering of this tetrahedral Al and Si arrangement in sillimanite might be an important factor leading to complications of the Al_2SiO_5 phase equilibria. Subsequently, other researchers (e.g., Holdaway 1971; Greenwood 1972; Saxena 1974) have also suggested that Al/Si disordering in sillimanite, which increases the configuration entropy, might have important effects on the phase relations of Al_2SiO_5 polymorphs.

Navrotsky et al. (1973) experimentally detected an enthalpy difference between untreated sillimanite and sillimanite heated at 1200–1700 °C under pressures of 1.6–2.3 GPa that they inferred to reflect Al/Si disordering. However, Holland and Carpenter (1986), using transmission electron microscopy (TEM), observed small glass inclusions in sillimanite samples heat-treated under conditions similar to those used by Navrotsky et al. (1973). They inferred that some transformation related to mullite [$Al_2(Al_{2+2x}Si_{2-2x})O_{10-x}$, where x = 0.17–0.59 (Cameron 1977), space group *Pbam* (No. 55)], which is more Al-rich

than sillimanite, had occurred as a result of partial melting at high temperatures, and that the enthalpy change detected by Navrotsky et al. (1973) might in part reflect the appearance of similar fine glass inclusions. These results imply that experimental investigation of the degree of Al/Si order in sillimanite at high temperatures is not simple; rather, careful differentiation between sillimanite and mullite, including glass phases, is very important.

However, sillimanite and mullite are difficult to distinguish because of the similarity of their crystal structures. Mullite has the same basic framework as sillimanite (i.e., AlO_4 octahedral chains and double SiO_4/AlO_4 tetrahedral chains), and its structure differs from that of sillimanite only by the disordered distribution of Al and Si in the tetrahedra and the existence of an additional tetrahedral site, which is coupled to the occurrence of oxygen vacancies (e.g., Fischer et al., 2012). In fact, Burnham (1963) reported that only a few atoms need to be slightly shifted or removed to create one phase from the other.

Moreover, the exact phase relation and the *P*–*T* boundary between the two phases is still not clear. Some researchers (e.g., Hariya et al. 1969) have suggested that there may be a complete solid solution series between sillimanite and mullite under certain high temperature and high pressure conditions, although it is relatively accepted that a miscibility gap exists at around $0.04 < x \leq 0.17$ in $Al_2(Al_{2+2x}Si_{2-2x})O_{10-x}$ (Cameron 1977). In addition, Fischer et al. (2015) newly reported a natural mineral, "sillimullite" that is intermediate between silimanite and mullite but different to both of them.

Furthermore, there are large inconsistencies among previous estimates of the phase boundary position on the *P*–*T* diagram (e.g., Holm and Kleppa 1966; Weill 1966; Kiseleva et al. 1983). The ambiguities regarding the phase relation between sillimanite and mullite

have prevented precise phase identifications and inhibited further investigations of Al/Si disordering in sillimanite.

Recently, Igami et al. (2017), using a synchrotron X-ray and high-resolution multiple-detector system developed by Toraya et al. (1996), successfully distinguished the X-ray diffraction (XRD) peaks of sillimanite and mullite in mixtures of these two minerals. In this study, therefore, we conducted experiments in which we treated sillimanite samples under various *P*–*T* conditions, and then we used the synchrotron XRD system and TEM-energy dispersive spectroscopy (EDS) to analyze the results. In particular, we re-examined the phase relation between sillimanite and mullite with consideration of the degree of Al/Si order in sillimanite by applying these methods to the investigation of submicroscopic textures and precise cell-parameter relations. On the basis of our results, we propose a new *P*–*T* diagram of the high-temperature region in the Al_2SiO_5 system.

Sample preparation

Starting material

As starting material (hereafter, STR), we used sillimanite crystals from the same sample (collected in Rundvågshetta, East Antarctica; RVH92011102A, Kawasaki et al. 1993, 2011) that we used in our previous experiments (Igami et al. 2017, 2018a). The XRD pattern of STR shows only sillimanite peaks, and its cell parameters are a = 7.4867(6), b = 7.6750(5), and c = 5.7720(5) Å (Igami et al., 2018). Its chemical composition, determined by scanning electron microscopy (SEM)-EDS, is $Al_{1.99}Fe_{0.01}Si_{1.00}O_5$ (Igami et al. 2017).

Under TEM, STR has no characteristic textures such as anti-phase boundary (APB) textures, lamellae, or inclusions (Igami et al. 2018a). The STR crystals were crushed, and impurities were removed under an optical microscope. Then, crystals of adequate size (~2 mm across) were picked out for use as single-crystal samples. The rest of the sample was ground to powder, and then powdered samples were loaded into 3-mm-diameter platinum capsules and then both sides of the capsule were squeezed flat for the heating experiment.

Heat treatments

Both the single-crystal and powdered samples were subjected to various temperatures and pressures. A muffle furnace was used for experiments at ambient pressure (1 atm), and an internally heated pressure vessel or piston-cylinder apparatus was used for experiments at high pressure (HP). Hereafter, experimental samples treated at temperature *T*, pressure *P*, for time *t* are designated as S_*T*-*P*-*t* (e.g., S_790°C-1atm-700h)

Muffle furnace. Both single-crystal and powdered samples were placed in a platinum crucible and heated in a muffle furnace (Nabertherm, LHT02/17 or Koyo, KBF314N1) at 1 atm and temperatures of 790 to 1530 °C for 1 to 1711 h. The temperature was measured with a $Pt_{70}Rh_{30}$–$Pt_{94}Rh_6$ (B-type) thermocouple placed at the top of the sample space in the furnace. A digital program controller maintained the run temperature within ±1 °C of the nominal value. After heating, the samples were allowed to cool at a cooling rate of ~10 °C/min. Igami et al. (2018a) previously observed some of these samples by TEM and used high angular resolution electron channeling X-ray spectroscopy (HARECXS) to determine

126 their Al/Si order parameters.

127

128 **Internally heated pressure vessel.** HP experiments at the pressure of 0.2 GPa were
129 performed in an internally heated pressure vessel (KOBELCO, Dr. HIP) at Chiba
130 University. A powdered sample in a Pt capsule or a single-crystal sample was placed in a
131 platinum wire cage in the internally heated pressure vessel and subjected to temperatures
132 from 1200 to 1400 °C. The pressurizing medium was Ar gas, and the pressure was
133 maintained within ±0.002 GPa of the nominal pressure of 0.2 GPa during all experiments.
134 The run temperature was monitored with a Pt–$Pt_{87}Rh_{13}$ (R-type) thermocouple in the vessel
135 and maintained within ±1 °C of the nominal value. After the heat treatment, samples were
136 allowed to cool at a cooling rate of ~100 °C /min.

137

138 **Piston-cylinder apparatus.** HP experiments at pressures of 0.5–2.5 GPa were performed
139 in a Boyd-England type piston-cylinder apparatus with a 1/2-inch-diameter cylinder and
140 piston (C&T Factory, PG-100) at Kyoto University. Powdered samples in Pt capsules were
141 placed in a MgO holder that was surrounded by graphite heaters, Pyrex glass and talc
142 sleeves, and subjected to temperatures from 1300 to 1500 °C. In these experiments,
143 single-crystal samples were not used. The pressure was maintained within ±0.2 GPa of the
144 nominal pressure during all experiments. The pressure calibration was previously carried
145 out using silica and enstatite phase transformations (Machida et al. 2017). The run
146 temperature was monitored with a Pt–$Pt_{87}Rh_{13}$ (R-type) thermocouple and a digital program
147 controller (CHINO, KP100c) maintained the temperature within ±1 °C of the nominal value.

The thermal gradient of the assembly was previously shown to be limited by an investigation of the run charge of an enstatite–diopside mixture (Machida et al. 2017). After the heat treatment, samples were allowed to cool at a cooling rate of ~100 °C/sec.

Experimental methods

Synchrotron powder XRD experiments

The powdered samples were analyzed by XRD using the multiple-detector system of Toraya et al. (1996) and the BL-4B$_2$ beamline at the Photon Factory of the High Energy Accelerator Research Organization, Tsukuba, Japan. The segmented intensity data were connected after adjustment for peak shifts and detector sensitivities (Ida 2005). The step interval for scanning was 0.005 or 0.010°, and the diffraction angles ranged from 8.000 to 150.000° 2θ. Because this XRD system is shared by several users, the measurements were performed over several intervals. Before each measurement interval, we therefore measured the Si powder standard (NIST SRM640c) and STR. The peak wavelength of the source X-ray beam was determined by analysis of the diffraction peak profiles of the Si powder (Ida et al. 2003). The wavelengths of the X-ray beam were determined to be 1.747061(11), 1.746881(11), 1.746985(10), 1.197419(7), and 1.197318(21) Å. Zero shift and eccentric error for each measurement interval were optimized by analysis of the diffraction peaks of STR.

TEM and scanning TEM observations

A focused ion beam (FIB) system (Thermo Fisher Scientific Quanta 200 3DS or

Helios NanoLab G3 CX) was used to prepare ultrathin sections of 16 single-crystal samples for TEM observations. The sections of crystal samples from the muffle furnace and internally heated pressure vessel treatments and the powdered samples from the piston-cylinder treatment were embedded in epoxy resin and then polished to a smooth surface. Using the FIB system, a predefined area (20–30 μm^2) was coated with Pt and then a Ga^+ ion gun was used to cut out the surrounding material to a depth of ~10 μm. Then the section was cut off, mounted on a TEM grid, and thinned to a thickness of ~150 nm using a Ga^+ ion beam at 30 kV with beam currents of 0.1–3 nA. In the final processing, a Ga^+ ion beam at 5 kV with a beam current of 48 pA was used to remove amorphous layers from the surface of the sections.

The samples were studied under a JEOL JEM-2100F transmission electron microscope operated at 200 kV at Kyoto University. TEM images were recorded by CCD cameras (Gatan, Orius 200D and 1000D). Selected area electron diffraction (SAED) patterns of mullite and sillimanite are similar, but show one important difference. In the case that a SAED pattern is indexed based on the standard cell of sillimanite, l = odd reflections are typical for sillimanite, but they are absent for mullite, as also described by Igami et al. (2018a). Samples were observed by dark field (DF) imaging taken from l = odd reflections of sillimanite as well as by bright field (BF) imaging.

Because mullite is slightly enriched in Al_2O_3 compared with sillimanite, chemical analyses were performed by annular dark-field scanning TEM (ADF-STEM) with X-ray mapping using a TEM equipped with annular STEM and EDS detectors (JEOL JED2300T). The acceptable angle of the STEM detector was set to approximately 50–150 mrad to

reflect the atomic numbers of the constituent elements (high-angle annular dark-field STEM image). Moreover, a simple k-factor method was used to evaluate the Al/Si ratio of some samples. The *k*-factor of Al-K to Si-K ($k_{Al/Si}$) was calibrated by using the STEM-EDS results for STR. By the STEM-EDS analysis of 12 different regions of STR, the $I_{(Al\text{-}K)}/I_{(Si\text{-}K)}$ X-ray count ratio converged to an average value of 2.09 with a standard error of 0.02. From this result, the *k*-factor was determined to be $k_{Al/Si} = 0.96$, to adjust the Al/Si compositional ratio of STR to 2.00. This *k*-factor includes the effect of X-ray absorption, but errors caused by the X-ray absorption effect were assumed to be small, because FIB was used to make the thickness of all of the TEM sections almost the same and because the absorption coefficients of Al-K and Si-K are similar.

Results and Discussion

Phase identification in high-resolution XRD patterns

The high-resolution XRD patterns of some heat-treated samples are similar to that of STR, but exhibited small new peaks and a broad glass halo, same as Igami et al. (2017). Peak positions of this newly appeared phase and sillimanite are so close to each other that they cannot be separated from their mixtures in laboratory XRD systems. Our XRD patterns indicate that the newly appeared phases show no diffraction peaks at the positions corresponding to the reflections with l = odd in the case of indexing based on the unit cell of sillimanite (Fig. 1, showing the case of S_1476°C-1atm-10h). This indicates that the appeared phase is changed in translational symmetry with half the size of the c axial length from sillimanite. It is most likely that mullite was formed from sillimanite with partial melting, although there remains a little possibility that the l = odd reflections are so weak that they cannot be detected in the multiphase patterns and the new phase might be a special mullite with doubled c parameter similar to the "sillimullite" described by Fischer et al. (2015). Some XRD patterns of HP-treated samples also included corundum peaks. The only detected phases in the XRD patterns were sillimanite, mullite, corundum, and glass. All detected crystalline phases in the samples are listed in Tables 1, 2. Clear mullite peaks were detected only in samples heated above 1200 °C.

Peak shifts of sillimanite and mullite detected in high-resolution XRD patterns

Compared with STR, the XRD patterns of heat-treated sillimanite at 1 atm seemed to show a slight peak shift as the treatment temperature increased (Fig. 2a). These peak

shifts, which were detected even though all of the XRD experiments were performed at room temperature, indicate slight changes in the crystal structure of the sillimanite except for thermal expansion or transformation to mullite. In samples treated by both heating and pressure, the XRD patterns also showed a shift in the mullite peak position (Fig. 2b). Thus, mullite seemed to change its crystallographic state as treatment temperature and pressure increased, and the pressure effect was likely more effective than the temperature effect as a cause of the structural change.

We evaluated these peak position differences by calculating the cell parameters of all of the experimental samples from the XRD patterns by least-squares fitting. Before the calculation, we carefully deconvoluted the peaks of sillimanite and mullite using the pseudo-Voigt function, taking advantage of the high angular resolution of the XRD system. The determined cell parameters are listed in Tables 1–2, and details are discussed later.

TEM observations of microtextures

Under TEM, the experimental samples showed various microtextures that were different from those of STR (Table 3). For example, TEM images and SAED patterns of S_1476°C-1atm-696h, the XRD pattern of which showed only mullite + glass, are shown in Figure 3. When SAED patterns are indexed according to the standard cell of sillimanite, reflections with l = odd (e.g., 021) are extinct, which indicates mullite. In this sample, many characteristic glass inclusions elongated in the direction of the *c*-axis of the host mullite were observed (Fig. 3a) with characteristic shapes bounded by the {110} prismatic planes of mullite (Fig. 3b). This texture is similar to that reported by previous TEM studies (e.g.,

248 Holland and Carpenter 1986; Raterron et al. 1999, 2000), and these inclusions should
249 correspond to the glass halo in the XRD patterns. STEM-EDS analysis using $k_{Al/Si}$ = 0.96 of
250 five different mullite regions without inclusions yielded an average Al/Si ratio = 3.02**(**10**)**,
251 which is consistent with the normal (3:2) mullite composition: $3Al_2O_3$ $2SiO_2$ (Al/Si = 3.00).
252 Figure 4 shows TEM images and SAED patterns of S_1450°C-1atm-1150h, which
253 was ~77% transformed to mullite + glass with ~23% remaining as sillimanite, as
254 determined by Igami et al. (2017). Two regions are seen in the DF image taken from the *l* =
255 odd reflection of sillimanite (Fig. 4a): a dark appearing mullite region and a bright
256 appearing sillimanite region. The mullite region has the same characteristics as
257 S_1476°C-1atm-696h (Fig. 3), whereas the residual sillimanite region exhibits textures like
258 anti-phase boundaries (APB-like texture) with a displacement vector of 1/2[001]. Glass
259 inclusions were observed along with these textures, although they were very fine. Holland
260 and Carpenter (1986) described similar APB-like textures in their TEM study.
261 APB-like textures visualized by DF-TEM imaging of *l* = odd reflections were also
262 observed in many samples that did not clearly show mullite regions. For example, Figure 5
263 shows an APB-like texture in S_1373°C-1atm-300h, ~24% of which was transformed to
264 mullite + glass with ~76% remaining as sillimanite, as determined by Igami et al. (2017). In
265 this TEM section, no clear mullite regions are present, but APB-like textures are observed
266 (Fig. 5b). The ADF-STEM image and X-ray map (Figs. 5d, e) clearly show that the regions
267 with these textures are more Al rich than the host sillimanite, and they are accompanied by
268 fine Si-rich inclusions. This observation indicates that the regions with APB-like texture are
269 not compositionally the same as the host but consist of mullite accompanied by fine

SiO_2-rich glass inclusions. These APB-like mullite textures were not observed in samples heated to less than 1140 °C; this result is consistent with our XRD results and with the mullitization temperature determined by Igami et al. (2017).

Figure 6 shows the TEM images of S_1400°C-1GPa-52h, which is composed of both sillimanite and mullite grains, identified by their SAED patterns. The mullite grains have fewer glass inclusions than those in samples heat-treated at 1 atm. STEM-EDS analysis of 10 different mullite regions yielded an average Al/Si ratio of 2.43(6), calculated using $k_{Al/Si} = 0.96$. This composition is intermediate between sillimanite (Al/Si = 2.00) and 3:2 mullite (Al/Si = 3.00), but it is within the mullite solid solution series proposed by Cameron (1977). Based on both the SAED and EDS results, this phase is referred to as siliceous mullite. The DF image of the *l* = odd reflection in a sillimanite grain showed APB-like textures but fewer glass inclusions than the samples heat treated at 1 atm. This result indicates that the regions with APB-like textures are also composed of siliceous mullite with relatively few glass inclusions. These findings support the inference of Hariya et al. (1969), deduced by XRD analysis, that siliceous mullite is formed at high pressures.

Cell parameter variation against treatment temperature

Figure 7 shows the determined cell parameters (Tabs. 1, 2) against treatment temperature. In the figure, the *b* axial length showed the most marked expansion, although the cell parameter that differs most between sillimanite and mullite is the *a* axial length. Igami et al. (2018a) determined that the Al/Si order parameter *Q* of the tetrahedral site in sillimanite, excluding mullite and glasses in the same sample. The *Q* value varies from 1

for total order to 0 to total disorder, and is given as $Q = 2p - 1$ in the case of stoichiometric sillimanite, where p is the probability of finding as Al (Si) atom on a Al (Si) site. The results of Igami et al. (2018a) shows that Q decreases continuously as the treatment temperature increases. Therefore, this characteristic change in the b axial length can be attributed to Al/Si disordering in sillimanite. We plotted the Q values determined by Igami et al. (2018a) against b axial length (Fig. 8) and found that the relation between Q and b tends to be negative and approximately linear, at least for $Q > 0.7$. According to Igami et al. (2018a), this range of Q corresponds to heating temperatures $T <$ ~1400 °C. It is not clear whether the relation is linear for $Q < 0.7$, corresponding to $T >$ ~1400 °C, but temperatures in this range are too high to be applicable to natural metamorphic processes. This result indicates that under metamorphic geological conditions, the order parameter Q of sillimanite can be roughly estimated from the b axial length of the sillimanite.

Sillimanite in HP-treated samples changes with increasing treatment temperature similarly to sillimanite in samples heated at 1 atm (Fig. 7, right panels). This result indicates that the pressure condition does not significantly affect Al/Si disordering and is in agreement with the assumption of Greenwood (1972). Two mullite samples (arrows in Fig. 7a, left panel) with a = ~7.52 Å plot between the sillimanite and mullite groups. These samples are 1 GPa-treated products, and the pressure effect that they exhibit is analyzed in detail below.

Cell parameter variations in relation to treatment pressure

Comparison of the a, b, and c axial lengths of sillimanite and mullite with

experimental pressure (Fig. 9) shows that increased pressure, but not increased temperature, caused shrinkage of the *a* axial length of mullite, but the *b* and *c* axial lengths did not show any remarkable change. This result is mostly consistent with the findings of Hariya et al. (1969). The *a* axial length of mullite is acknowledged to increase almost linearly with increases in the Al component (e.g., Cameron 1977); thus, Hariya et al. (1969) estimated the chemical composition of HP experimental samples from the relation between *a* axial length and pressure in analytical results for mullite obtained previously. Our results show that the *a* axial length in the HP samples is about intermediate between that of sillimanite and 3:2 mullite, consistent with our STEM-EDS chemical analysis results (Al/Si = 2.43(6) for S_1400°C-1GPa-52h). As Hariya et al. (1969) pointed out, our analytical results also suggest that the SiO_2 component in mullite increases with increasing experimental pressure.

Cell parameter relationships between sillimanite and mullite

To gain an overview of cell parameter relationships between sillimanite and mullite, Hariya et al. (1969) plotted sillimanite and mullite cell parameters on the *V*–*a* plane, where *a* is *a* axial length and *V* is unit cell volume. They argued on the basis of the continuity of the plots on the *V*–*a* plane that structural change is continuous between sillimanite and mullite. However, as discussed above, expansion of the *b* axis of sillimanite is caused by Al/Si disordering with increasing temperature, and shrinkage the *a* axis of mullite is caused by an increased in the SiO_2 component with increasing pressure. To emphasize these two factors, we projected data onto the *b*–*a* plane where *b* is *b* axial length (Fig. 10). The *b*–*a* projection does not include information on the *c* axis, but *c* axis changes caused by

mullitization, Al/Si disordering in sillimanite, or changes in the Al_2O_3 component of mullite are very small (Figs. 7, 9). The cell parameters of siliceous mullite obtained by the 1 GPa treatments in this study do not match with those of "sillimullite" by Fischer et al. (2015) (Fig. 10). Moreover, they do not plot on the tie line connecting ordered sillimanite and mullite in the *b*–*a* plane projection, whereas the cell parameters of sillimullite is on the tie line reflecting its intermediate feature in crystallography. This result suggests that the structural changes between ordered sillimanite and mullite in heat-treatment are not continuous and not via "sillimullite" structure. Instead, the plots can be divided into two groups: one group consists of phases with various *a* axial lengths but similar *b* axial lengths (*b* = ~7.69 Å) (Group A), and the other consists of phases with various *b* axial lengths but similar *a* axial lengths (*a* = ~7.485 Å) (Group B). Group A consists of mullite with various compositions, and Group B consists of sillimanite with various degrees of Al/Si disorder. If we extend the two lines from Group B and Group A, they cross at around *a* = ~7.49 Å, *b* = ~7.69 Å; such a crossover point implies a phase with a stoichiometric Al_2SiO_5 composition and disordered Al and Si, that is, completely disordered sillimanite. However, this hypothetical phase requires at least *T* > ~1700 °C and *P* > ~2 GPa, based on the results of this study, so it is unsurprising that this phase has never been observed, including in the present experiment.

In contrast to this conclusion, Hariya et al. (1969) argued that a complete solid solution series exists between sillimanite and mullite at high pressures and high temperatures. However, their result should be reconsidered in light of the resolution of the XRD system used. Inspection of the XRD patterns shown by Hariya et al. (1969) indicates

that the resolution of their XRD system might have been too low to distinguish between sillimanite and mullite in samples in which they coexisted. For example, they show that a sample treated at 1500 °C and 1.1 GPa for 20 h had cell parameters intermediate between those of sillimanite and mullite. In this study, however, we detected two phases: partially disordered sillimanite ($b \approx 7.68$ Å) and siliceous mullite ($a \approx 7.52$ Å) in a sample treated under similar experimental conditions (S_1500°C-1.0GPa-2.5h). In Figure 10, the cell parameters of the sample of Hariya et al. (1969) plots almost on a tie line connecting our two detected phases. This result suggests that the sample of Hariya et al. (1969) might have contained both mullite and sillimanite, but they detected them as a single phase. Thus, the cell parameters that they reported are likely, in reality, to be weighted means of the cell parameters of separate sillimanite and mullite phases in the sample.

Mullitization boundary on *P–T* diagram

If there is not a complete solid solution series between sillimanite and mullite under normal geological conditions, as we assert here, a transformation boundary between them should exist on the *P–T* diagram of the Al_2SiO_5 system. To estimate the position of this boundary, we plotted the experimental results of this study and the mullitization temperature of 1200 °C at 1 atm, determined by Igami et al. (2017), on the *P–T* diagram (Fig. 11). In addition, we re-examined representative previous heat-treatment studies.

Holland and Carpenter (1986), who treated sillimanite samples at 1300–1620 °C and 1.8–2.0 GPa, reported abundant APBs or APB-like defects with glass inclusions. They

interpreted the cause of these textures to be both continuous enrichment in Al_2O_3 and Al/Si disordering. In our samples, however, similar microtextures were identified by STEM-EDS to be fine mullite, and their XRD patterns indicated that mullite formed discontinuously from sillimanite. Our results imply a compositional gap between sillimanite and mullite in the SiO_2–Al_2O_3 system at 1.8–2.0 GPa, different from the schematic phase diagram proposed by Holland and Carpenter (1986). We consider that the samples that they described as having abundant APBs may have started to transform to mullite (Fig. 11).

Raterron et al. (2000) also observed glass inclusions and dislocations in sillimanite treated at 1675 °C and 0.5–3.0 GPa, and they interpreted these textures in terms of a continuous solid-solution model between sillimanite and mullite. We agree with their conclusion that mullite has a variable composition at different pressures and temperatures, but we think that a compositional gap exists between sillimanite and mullite. The glass inclusions and other textures observed by them are similar to those observed in the present HP-samples that show peaks of both sillimanite and mullite in their XRD patterns. We infer that all of their experimental samples had started to transform to mullite (Fig. 11).

Navrotsky et al. (1973) measured the enthalpy of solution of heat-treated samples, and found a distinct decrement of the enthalpy of solution in samples treated at >1400 °C and 1.6–2.3 GPa, compared with unheated sillimanite. They concluded that the enthalpy change was due to Al/Si disordering in stoichiometric sillimanite, but as pointed out by Holland and Carpenter (1986), this result was more likely caused by mullitization. At experimental pressures of 1.6–2.3 GPa, 1400 °C should be in the mullitization region on the *P*–*T* diagram (Fig. 11).

The mullitization boundary estimated from our experiments is shown by a broad shaded band in Figure 11. Mullitization is a very sluggish reaction, so the dP/dT gradient may be even steeper than the indicated line because the duration of our high-pressure experiments was much shorter than that of the 1 atm experiments of Igami et al. (2017).

Figure 11 also shows the mullitization boundaries estimated by calorimetric studies on the *P–T* diagram (Holm and Kleppa 1966; Weill 1966; Kiseleva et al. 1983). Although our determined boundary is closest to the result of Holm and Kleppa (1966) among the three examples, Anderson and Kleppa (1969) re-evaluated the result of Holm and Kleppa (1966) and determined it to be partly inaccurate. Thus, the consistency between our result and that of Holm and Kleppa (1966) might be of little importance. The slope of the boundary estimated by this study is steeper than that of Weill (1966) or Kiseleva et al. (1983), which may imply expansion of the mullite stability field caused by the effect of pressure-induced compositional changes. Weill (1966) and Kiseleva et al. (1983) calculated the phase boundaries for mullite with a fixed composition.

Al/Si order parameter of stoichiometric sillimanite in *P–T* diagram

Our XRD results revealed that sillimanite shows a continuous increase in Al/Si disorder with increasing treatment temperatures. Igami et al. (2018a) previously determined the Al/Si order parameter Q of sillimanite in some of the studied samples. These Q values are reliable because precipitated phases (mullite and glasses) were surely excluded from the analytical regions examined by TEM. In addition, our XRD results show that the pressure effect on the Q value may be negligible (Fig. 7). In Figure 12, we show Q values of

424 sillimanite as a contour on a *P*–*T* diagram, where the *Q* values are expressed by the
425 Bragg-Williams model as a function of temperature and independent of pressure: $Q\ (T_c/T) =$
426 $1/2\ \ln[(1 + Q) / (1 - Q)]$, where T_c = 1727 °C (Igami et al. 2018a). Thus, the *Q* contour line
427 is projected vertically onto the *P*-*T* plane.

428 This figure shows that the *Q* value at the aluminosilicate triple point is much higher
429 than *Q* = 0.975. Similarly, the *Q* value at the sillimanite–andalusite boundary is higher than
430 ~0.95. Therefore, the effect of Al/Si disordering on the triple point equilibrium and the
431 sillimanite–andalusite boundary seem to be negligible. In contrast, the sillimanite on the
432 sillimanite–kyanite boundary at high temperatures is in a relatively low ordered state,
433 which indicates that the stability field of sillimanite should expand toward that of kyanite.
434 These results agree with the conclusions of previous theoretical studies (e.g., Saxena 1974).
435

436 **Implications**

437 The present experimental results imply that submicrometric textures and
438 crystallographic features of sillimanite and mullite may be useful for investigating the
439 thermal history of natural samples, in particular, rocks produced by ultra-high-temperature
440 metamorphism.

441 For example, Aramaki (1961) reported that sillimanite in pelitic xenoliths from
442 Asama Volcano in Japan have cell parameters *a* = 7.498(3), *b* = 7.690(3), and *c* = 5.797(3)
443 Å, which are near the crossover point shown in Figure 10. Cameron and Ashworth (1972)
444 studied the same Asama sillimanite and reported slightly different cell parameters: *a* =
445 7.4963(4), *b* = 7.6851(4), and *c* = 5.7764(3) Å. Recently, we showed that mullite with a

submicrometric core-rim texture coexists with sillimanite in aluminosilicates from the same locality (Igami et al. 2018b); thus, the previously reported cell parameters can be interpreted as resulting from the presences of double sillimanite and mullite peaks, similar to our interpretation of the results of Hariya et al. (1969). Under this assumption, the *b* axial length of sillimanite reported by Cameron and Ashworth (1972) seems to be rather large, an indication that the Al/Si arrangement is considerably disordered. This finding is consistent with the TEM observation of Igami et al. (2018b) that APBs with a displacement vector of 1/2[001] were abundant in the sample. The cell parameters reported by Aramaki (1961) have no clear explanation, but their differences with those reported by Cameron and Ashworth (1972) probably reflect a difference in the abundance ratio of sillimanite and mullite. Although the low Al/Si order parameter of this sillimanite cannot be directly associated with temperature in Figure 12, because this low ordered state was probably caused by the transformation of mullite to sillimanite (Igami et al. 2018b), the sample might have reached temperatures around the mullitization boundary.

As in the case of this Asama aluminosilicate example, many interesting characteristics of sillimanite and mullite samples may be overlooked. Investigations of sillimanite that take account of the results of this study can yield new information about thermal histories in high-temperature regions above 1000 °C that is easy to be lost in general.

Acknowledgments

We are grateful to Akira Tsuchiyama, Norimasa Shimobayashi, Takao Hirajima, Tetsuo Kawakami, and Masao Kitamura for critical discussions. We sincerely thank Toshisuke Kawasaki for providing the samples. We also thank Yu Kodama, Tatsuya Osako Yuh-Chyuan Chang, and Tomoki Taguchi for their help with the experiments conducted at the Photon Factory. This manuscript was greatly improved by outstanding comments by Reinhard X. Fischer and an anonymous reviewer. This work was supported by JSPS KAKENHI Grant Number JP16H06348 to AM.

References

Anderson, P.A.M., and Kleppa, O.J. (1969) The thermochemistry of the kyanite-sillimanite equilibrium. American Journal of Science, 267, 285–290.

Aramaki, S. (1961) Sillimanite and cordierite from volcanic xenoliths. American Mineralogist, 46, 1154–1165.

Bish, D.L., and Burnham, G.W. (1992) Rietveld refinement of the crystal structure of fibrolitic sillimanite using neutron powder diffraction data. American Mineralogist, 77, 374–379.

Burnham, C.W. (1963) Refinement of the crystal structure of sillimanite. Zeitschrift für Kristallographie, 118, 127–148.

Cameron, W.E. (1977) Mullite; a substituted alumina. American Mineralogist, 62, 747–755.

Cameron, W.E., and Ashworth, J.R. (1972) Fibrolite and its relationship to sillimanite. Nature Physical Science, 235, 134.

Fischer, R.X., Gaede-Köhler, A., Birkenstock, J., and Schneider, H. (2012) Mullite and mullite-type crystal structures. International Journal of Materials Research, 103, 402–407.

Fischer, R.X., Tikhonova, V., Birkenstock, J., Fischer, L.A., Herrmann, K., Mengel, K., and Schneider, H. (2015). A new mineral from the Bellerberg, Eifel, Germany, intermediate between mullite and sillimanite. American Mineralogist, 100, 1493–1501.

Greenwood, H.J. (1972) AlIV -SiIV disorder in sillimanite and itseffect on phase relations of the aluminum silicate minerals. Geological Society of America, Memoir, 132,

553–571.

Hariya, Y., Dollase, W.A., and Kennedy, G.C. (1969) An experimental investigation of the relationship of mullite to sillimanite. American Mineralogist, 54, 1419–1441.

Holdaway, M.J. (1971) Stability of andalusite and the aluminum silicate phase diagram. American journal of science, 271, 97–131.

Holland, T.J.B., and Carpenter, M.A. (1986) Aluminium/ silicon disordering and melting in sillimanite at high pressures. Nature, 320, 151–153.

Holm, J.L., and Kleppa, O.J. (1966) The thermodynamic properties of the aluminum silicates. American mineralogist, 51, 1608–1622.

Ida, T. (2005) Connection of segmented intensity data measured with a multiple-detector system for powder diffractometry. Journal of Applied Crystallography, 38, 795–803.

Ida, T., Hibino, H., and Toraya, H. (2003) Deconvolution of instrumental aberrations for synchrotron powder X-ray diffractometry. Journal of Applied Crystallography, 36, 181–187.

Igami, Y., Ohi, S., and Miyake, A. (2017) Sillimanite–mullite transformation observed in synchrotron X-ray diffraction experiments. Journal of the American Ceramic Society, 100, 4928–4937.

Igami, Y., Kuribayashi, T., and Miyake, A. (2018a) Determination of Al/Si order in sillimanite by high angular resolution electron channeling X-ray spectroscopy, and implications for determining peak temperatures of sillimanite. American mineralogist, 103, 944–951.

Igami, Y., Miyake, A., and Shimobayashi, N. (2018b) Mullite in a buchite from Asama

volcano and its sub-micrometric core-rim texture with sillimanite. Journal of Mineralogical and Petrological Sciences, 113, 198–206.

Kawasaki, T., Ishikawa, M., and Motoyoshi, Y. (1993) A preliminary report on cordierite-bearing assemblages from Rundvågshetta, Lützow-Holm Bay, East Antarctica: Evidence for a decompressional *P*-*T* path? Proceedings of NIPR Symposium of Antarctic Geosciences, 6, 47–56.

Kawasaki, T., Nakano, N., and Osanai, Y. (2011) Osumilite and a spinel + quartz association in garnet–sillimanite gneiss from Rundvågshetta, Lützow-Holm Complex, East Antarctica. Gondwana Research, 19, 430–445.

Kiseleva, I.A., Ostapenko, G.T., Ogorodova, L.P., Toper, N.D., and Timoshkova, L.P. (1983) High-temperature calorimetry data on the equilibrium between andalusite, kyanite, sillimanite, and mullite. Geochemistry International, 20, 17–26.

Machida, S., Kogiso, T., and Hirano, N. (2017) Petit-spot as definitive evidence for partial melting in the asthenosphere caused by CO_2. Nature Communications, 8, 14302.

Navrotsky, A., Newton, R.C., and Kleppa, O.J. (1973) Sillimanite-disordering enthalpy by calorimetry. Geochimica et Cosmochimica Acta, 37, 2497–2508.

Peterson, R.C., and McMullan, R.K. (1986) Neutron diffraction studies of sillimanite. American Mineralogist, 71, 742–745.

Raterron, P., Carpenter, M., and Doukhan, J.C. (1999) Sillimanite mullitization: ATEM investigation and point defect model. Phase transitions, 68, 451–500.

Raterron, P., Carpenter, M., and Doukhan, J.C. (2000) ATEM investigation of experimentally annealed sillimanite: new constraints for the SiO_2 - Al_2O_3 join.

Mineralogical Magazine, 64, 247–254.

Saxena, S.K. (1974) Order disorder in sillimanite. Contributions to Mineralogy and Petrology, 45, 161–167.

Toraya, H., Hibino, H., and Ohsumi, K. (1996) A new powder diffractometer for synchrotron radiation with a multiple-detector system. Journal of Synchrotron Radiation, 3, 75–83.

Weill, D.F. (1966) Stability relations in the Al_2O_3–SiO_2 system calculated from solubilities in the Al_2O_3–SiO_2–Na_3AlF_6 system. Geochimica et Cosmochimica Acta, 30, 223–237.

Winter, J.K., and Ghose, S. (1979) Thermal expansion and high-temperature crystal chemistry of the Al_2SiO_5 polymorphs. American Mineralogist, 64, 573–586.

Zen, E.A. (1969) The stability relations of the polymorphs of aluminum silicate; a survey and some comments. American Journal of Science, 267, 297–309.

Table titles and figure captions

Tables

Table 1.

Cell parameters of detected crystalline phases in the experimental samples at 1 atm.

Table 2.

Cell parameters of detected crystalline phases in the experimental samples at high pressures.

Table 3.

TEM observation results.

Figures

Figure 1.

Powder X-ray diffraction patterns of STR (lower) and S_1476˚C-1atm-10h (upper). (**a**) Whole diffraction patterns. All the peaks in STR are reflections of sillimanite. The label of "Sil 210" indicates 210 reflection of sillimanite, which is enlarged in Figure 2. (**b**)(**c**) Enlargements of representative peaks. The reflections of 121, 211 and 220 of sillimanite are shown from both STR and S_1476˚C-1atm-10h (solid arrows). On the assumption that the space group of the new appeared phase is *Pbnm* same with sillimanite, 121, 211 and 220 reflection peaks are predicted to appear at 2θ = 34.51, 34.83 and 37.88˚, respectively

578 (dotted arrows). In the pattern of S_1476˚C-1atm-10h, there are a clear peak
579 corresponding to 220 reflection (c), but no peak corresponding to 121 or 211 which is the *l*
580 = odd reflections (b).
581
582 **Figure 2.**
583 XRD peak shifts induced by (**a**) high temperature and (**b**) high temperature and high
584 pressure treatments. The peaks are labeled with their Miller indices, preceded by sil for
585 sillimanite and mul for mullite. (**a**) XRD patterns of STR, S_1000°C-1atm-700h,
586 S_1090°C-1atm-1255h, S_1200°C-1atm-500h, S_1290°C-1atm-60h,
587 S_1373°C-1atm-1711h, and S_1476°C-1atm-10h, arranged in order of treatment
588 temperature. (**b**) XRD patterns of 1373°C-1atm-300h, 1400°C-0.2GPa-19h, and
589 1400°C-1.0GPa-2.5h, arranged in order of treatment pressure.
590
591 **Figure 3.**
592 TEM images and SAED patterns of S_1476°C-1atm-696h. (**a**) BF-TEM image and SAED
593 pattern on the projection of [100]. In case of indexing using sillimanite cell parameters, the
594 *l* = odd reflections are extinct, which means the samples completely transformation to
595 mullite. (b) BF-TEM image and SAED patterns on the projection of [001]. SAED pattern
596 taken from an inclusion (lower right), shows glass halo.
597
598 **Figure 4**.
599 S/TEM-EDS images of S_1450°C-1atm-1150h. (**a**) DF-TEM image of the section taken

600 from the g = 101 reflection of sillimanite. (**b**) SAED pattern of the same area. (**c**)
601 ADF-STEM images. (**d**) X-ray map obtained by dividing $I_{Al\text{-}K}$ by $I_{Si\text{-}K}$.
602
603 **Figure 5.**
604 S/TEM-EDS images of S_1373°C-1atm-300h. (**a**) BF-TEM image and (**b**) DF-TEM image
605 taken from the *g* = 021 reflection. (**c**) SAED pattern of the same area. (**d**) ADF-STEM
606 image. (**e**) X-ray map obtained by dividing $I_{Al\text{-}K}$ by $I_{Si\text{-}K}$.
607
608 **Figure 6.**
609 TEM images and SAED patterns of S_1400°C-1GPa-52h. (**a**) BF-TEM image of a section
610 containing two grains. (**b**) Enlarged BF-TEM image of the region enclosed by a dotted
611 rectangle in (a) and the SAED pattern of the same area, which shows a mullite pattern.
612 There are fewer glass inclusions than in the samples heat treated at 1 atm. (**c**) Enlarged BF-
613 and DF-TEM images of the region enclosed by a second dotted rectangle in (a) and the
614 SAED pattern of the same area. The SAED pattern shows the *l* = odd reflections of
615 sillimanite, and the DF image is taken from the g = 211 reflection of sillimanite. In this
616 grain, an APB-like texture with few glass inclusions was observed.
617
618 **Figure 7.**
619 (**a**) *a*, (**b**) *b*, and (**c**) *c* axial lengths of sillimanite and mullite in relation to treatment
620 temperature. To simplify comparison with sillimanite, the *c* axis of mullite is treated as the
621 twice length. The panels on the right are enlargements of the areas between the dashed

622 horizontal lines in the left panels. Arrows in the left panel of (a) indicate mullite in the 1
623 GPa treatment product.
624
625 **Figure 8.**
626 Order parameter *Q* values from Igami et al. (2018a) plotted against *b* axial lengths
627 determined in this study; *Q* and *b* tend to be negatively correlated.
628
629 **Figure 9.**
630 (**a**) *a*, (**b**) *b*, and (**c**) *c* axial lengths of sillimanite and mullite plotted against experimental
631 pressure.
632
633 **Figure 10.**
634 Projection of our results on the *b*–*a* plane. A continuous relationship between ordered
635 sillimanite and mullite is not observed. Instead, the plots can be divided into Group A and
636 Group B with a hypothetical crossover point at *a* = ~7.49 Å, *b* = ~7.69 Å. The
637 1500°C-1.1GPa-20h product reported by Hariya et al. (1969) (rhombus), lies roughly on the
638 tie line (dotted line) between the two phases that we detected in a similar experimental
639 sample in this study (S_1500°C-1.0GPa-2.5h, shown by large circle and large square). If
640 we assume that the cell parameters of Asama sillimanite (Cameron and Ashworth 1972) are
641 weighted means of sillimanite and mullite parameters, then the *b* axial length of sillimanite
642 seems to be relatively large compared with the STR of this study, indicating a disordered
643 Al/Si arrangement.

644

645 **Figure 11.**

646 *P–T* diagram showing the phase relation between sillimanite and mullite in the results of
647 this study and previous studies. In this study, open circles indicate that mullite is present,
648 and filled circles indicate that it is absent. Half-filled circles indicate that presence of
649 mullite is slight or unclear. The mullitization temperature at 1 atm (1200 °C) determined by
650 reaction kinetics analysis (Igami et al., 2017) is plotted by a cross. Previous studies reported
651 that some experimentally heated samples show intermediate feature between sillimanite and
652 mullite (hatched symbols), but their samples may have coexistence of mullite and
653 sillimanite, according to comparison of the original description with our results. The broad
654 shaded band shows the mullitization boundary estimated in this study. Mullitization
655 boundaries estimated by previous studies are also shown.

656

657 **Figure 12.**

658 *P–T* diagram of the Al_2SiO_5 system showing the contour of the *Q* value of sillimanite.
659 Phase boundaries between kyanite, andalusite, and sillimanite follow Holdaway (1971).
660 The *Q* values are expressed as a function of temperature, and independent of pressure, in
661 accordance with the Bragg-Williams model (Igami et al. 2018a): $Q\ (T_c/T) = 1/2\ \ln[(1 + Q) /$
662 $(1 – Q)]$, where T_c = 1727 °C. The stability field of sillimanite should expand toward that of
663 kyanite with increasing temperature because of Al/Si disordering (expressed schematically
664 by the curved dashed line).

665

Sample Name	Sillimanite			Mullite		
	a (Å)	*b* (Å)	*c* (Å)	*a* (Å)	*b* (Å)	*c* (Å)
S_790˚C-1atm-700h	7.4850(3)	7.6742(2)	5.7719(3)	-	-	-
S_890˚C-1atm-700h	7.4855(2)	7.67446(13)	5.7724(2)	-	-	-
S_1000˚C-1atm-700h	7.4859(2)	7.67446(12)	5.7722(2)	△	△	△
S_1040˚C-1atm-700h	7.4858(2)	7.67490(11)	5.7722(2)	△	△	△
S_1090˚C-1atm-1255h	7.4861(2)	7.67497(13)	5.7720(2)	△	△	△
S_1140˚C-1atm-1512h	7.4867(2)	7.67586(11)	5.7722(2)	△	△	△
S_1200˚C-1atm-500h	7.4861(2)	7.67566(15)	5.7717(2)	△	△	△
S_1240˚C-1atm-144h	7.4869(2)	7.67642(12)	5.7717(2)	△	△	△
S_1239˚C-1atm-785h	7.4877(2)	7.67672(13)	5.7720(3)	7.5403(6)	7.6880(9)	2.8852(6)
S_1290˚C-1atm-60h	7.4865(2)	7.67698(13)	5.7717(2)	7.5513(10)	7.6923(8)	2.8867(8)
S_1373˚C-1atm-70h	7.4874(2)	7.6788(2)	5.7711(2)	7.5441(5)	7.6905(3)	2.8846(3)
S_1373˚C-1atm-300h	7.4873(2)	7.67968(13)	5.7718(2)	7.5423(4)	7.6916(2)	2.8855(2)
S_1373˚C-1atm-1711h	7.4884(2)	7.6809(2)	5.7717(3)	7.5385(4)	7.6912(3)	2.8852(2)
S_1476˚C-1atm-1h	7.4873(2)	7.6810(2)	5.7713(2)	7.5480(4)	7.6889(6)	2.8853(4)
S_1476˚C-1atm-10h	7.4886(2)	7.68245(12)	5.7719(2)	7.5390(5)	7.6914(3)	2.8858(3)
S_1476˚C-1atm-90h	7.4903(4)	7.6835(3)	5.7707(5)	7.5440(2)	7.69141(15)	2.88502(11)
S_1476˚C-1atm-696h	-	-	-	7.5408(2)	7.6919(2)	2.88457(11)
S_1530˚C-1atm-5h	7.4879(2)	7.6828(2)	5.7712(2)	7.5496(3)	7.6888(3)	2.8853(2)
S_1530˚C-1atm-20h	7.4898(3)	7.6854(3)	5.7714(3)	7.5484(4)	7.6902(3)	2.8856(2)
S_1530˚C-1atm-60h	-	-	-	7.5436(5)	7.6927(3)	2.8848(3)

Note: ○, detected; △, slightly detected; -, not detected

Corundum
-
-
-
-
-
-
-
-
-
-
-
-
-
-
-
-
-
-
-
-

Sample Name	Sillimanite			Mullite		
	a (Å)	*b* (Å)	*c* (Å)	*a* (Å)	*b* (Å)	*c* (Å)
S_1200˚C-0.2GPa-45h	7.4869(2)	7.67690(13)	5.7714(2)	△	△	△
S_1300˚C-0.2GPa-41.5h	7.4882(2)	7.6799(2)	5.7710(3)	7.5374(7)	7.6887(5)	2.8856(5)
S_1400˚C-0.2GPa-19h	7.4884(2)	7.68184(11)	5.7703(3)	7.5401(6)	7.6894(5)	2.8833(5)
S_1400˚C-1GPa-2.5h	7.4866(2)	7.68184(13)	5.7701(4)	7.5200(3)	7.6906(2)	2.8840(3)
S_1500˚C-1GPa-2.5h	7.4874(2)	7.68280(14)	5.7700(4)	7.5219(5)	7.6901(3)	2.8843(5)
S_1300˚C-2.5GPa-24h	7.48767(15)	7.67745(11)	5.7717(2)	-	-	-
S_1400˚C-2.4GPa-22h	7.4913(2)	7.6806(2)	5.7716(2)	-	-	-

Note: ○, detected; △, slightly detected; -, not detected

Corundum
○
○
○
-
-
○
○

Sample name (Section No.)	Glass inclusion	APB-like texture	Mullite region
S_1530°C-1 atm-5h (1)	◎	◎	○
S_1476°C-1 atm-696h (1)	◎	-	◎
S_1476°C-1 atm-90h (1)	◎	-	◎
S_1476°C-1 atm-10h (1)	◎	◎	○
S_1476°C-1 atm-1h (1)	○	○	○
S_1476°C-1 atm-1h (2)	○	○	-
S_1450°C-1 atm-1150h (1)	◎	◎	◎
S_1373°C-1 atm-1711h (1)	○	○	-
S_1373°C-1 atm-1711h (2)	◎	◎	-
S_1373°C-1 atm-300h (1)	◎	◎	-
S_1373°C-1 atm-300h (2)	○	△	-
S_1373°C-1 atm-300h (3)	-	-	-
S_1373°C-1 atm-70h (1)	△	△	-
S_1290°C-1 atm-60h (1)	○	○	-
S_1290°C-1 atm-60h (2)	○	-	○
S_1239°C-1 atm-785h (1)	△	△	-
S_1140°C-1 atm-1512h (1)	-	-	-
S_1140°C-1 atm-1512h (2)	-	-	-
S_1140°C-1 atm-1512h (3)	-	-	-
S_1090°C-1 atm-1255h (1)	-	-	-
S_1400°C-0.2 GPa-19h (1)	◎	◎	-
S_1400°C-1.0 GPa-52h (1)	△	○	◎
S_1400°C-2.4 GPa-22h (1)	-	○	-
S_1400°C-2.4 GPa-22h (2)	△	○	-

S_1400°C-2.4 GPa-22h (3)	△	-	-
Starting material (1)	-	-	-
Starting material (2)	-	-	-

Note: ◎, abundantly observed; ○, observed; △, rarely observed; -, never

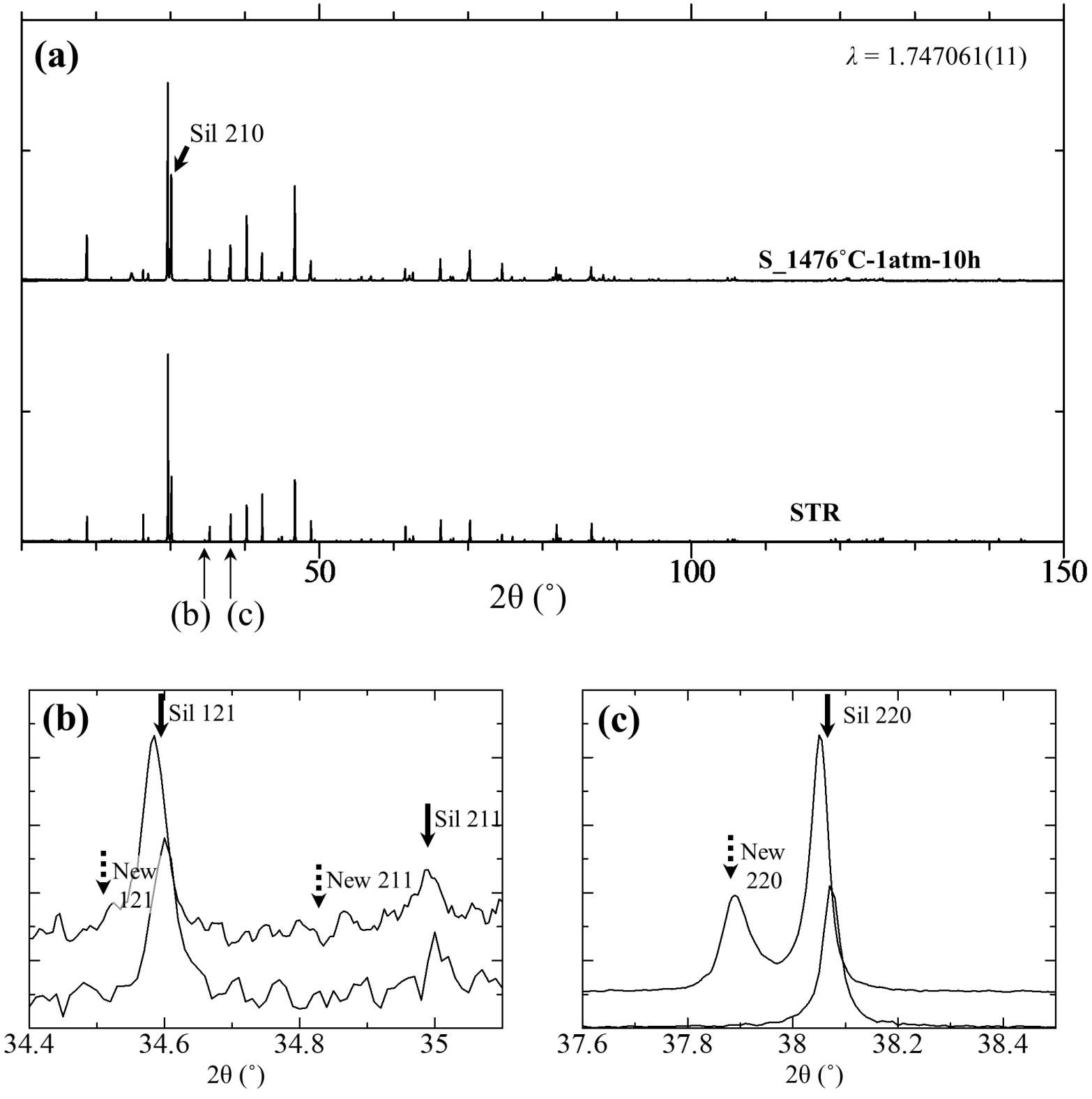
(a)
λ = 1.747061(11)
Sil 210
S_1476˚C-1atm-10h
STR
50
100
150
2θ (˚)
(b)
(c)
(b)
Sil 121
Sil 211
New 121
New 211
34.4
34.6
34.8
35
2θ (˚)
(c)
Sil 220
New 220
37.6
37.8
38
38.2
38.4
2θ (˚)

Figure 1

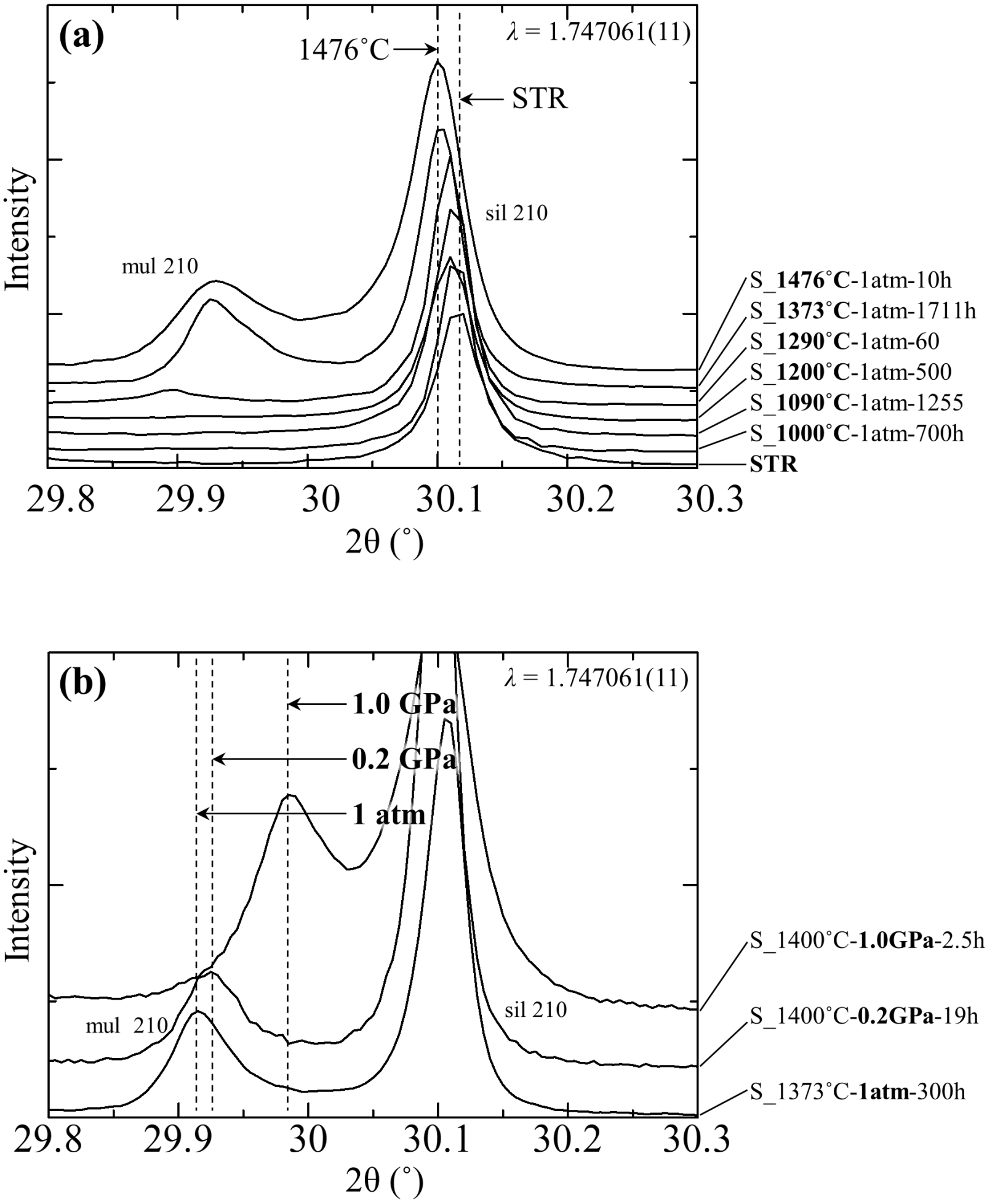
(a)
λ = 1.747061(11)
1476˚C
STR
sil 210
mul 210
Intensity
S_1476˚C-1atm-10h
S_1373˚C-1atm-1711h
S_1290˚C-1atm-60
S_1200˚C-1atm-500
S_1090˚C-1atm-1255
S_1000˚C-1atm-700h
STR
29.8
29.9
30
30.1
30.2
30.3
2θ (˚)
(b)
λ = 1.747061(11)
1.0 GPa
0.2 GPa
1 atm
Intensity
mul 210
sil 210
S_1400˚C-1.0GPa-2.5h
S_1400˚C-0.2GPa-19h
S_1373˚C-1atm-300h
29.8
29.9
30
30.1
30.2
30.3
2θ (˚)

Figure 2

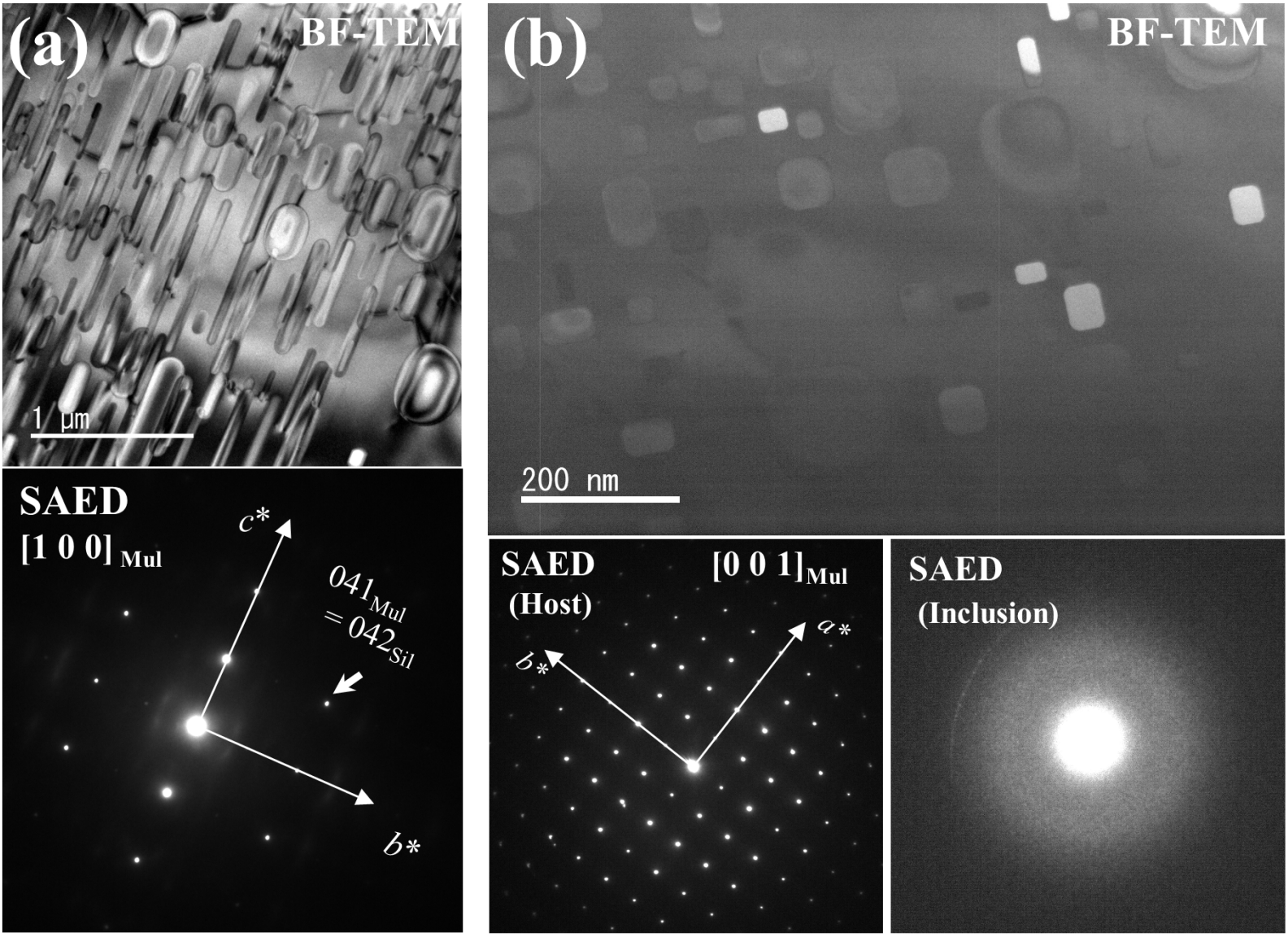
(a)
BF-TEM
1 μm
(b)
BF-TEM
200 nm
SAED
[1 0 0] Mul
c*
041Mul
= 042Sil
b*
SAED
(Host)
[0 0 1]Mul
a*
b*
SAED
(Inclusion)

Figure 3

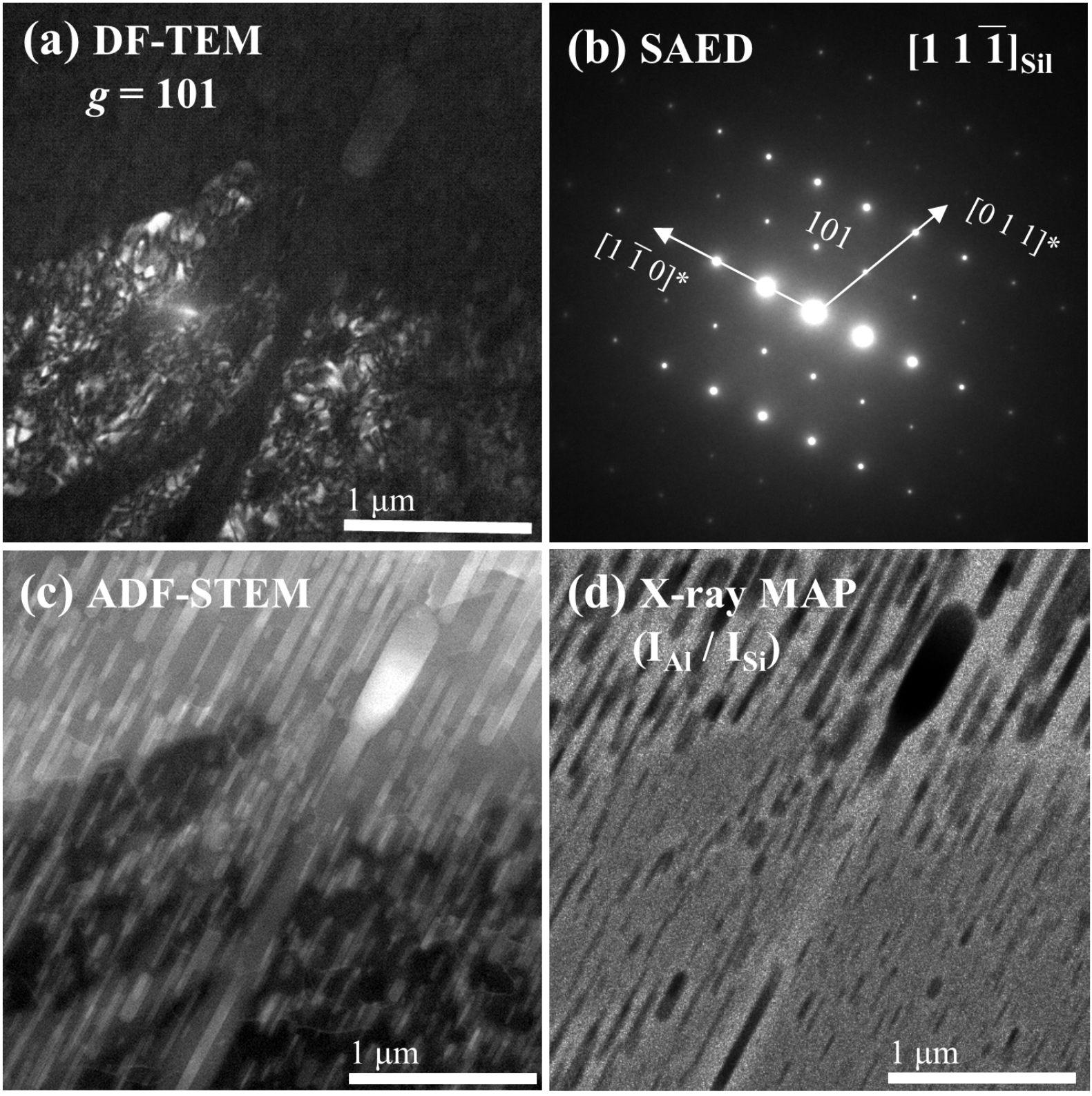
(a) DF-TEM
g = 101
1 μm
(b) SAED
[1 1 $\bar{1}$]Sil
[1 $\bar{1}$ 0]*
101
[0 1 1]*
(c) ADF-STEM
1 μm
(d) X-ray MAP
(I_{Al} / I_{Si})
1 μm

Figure 4

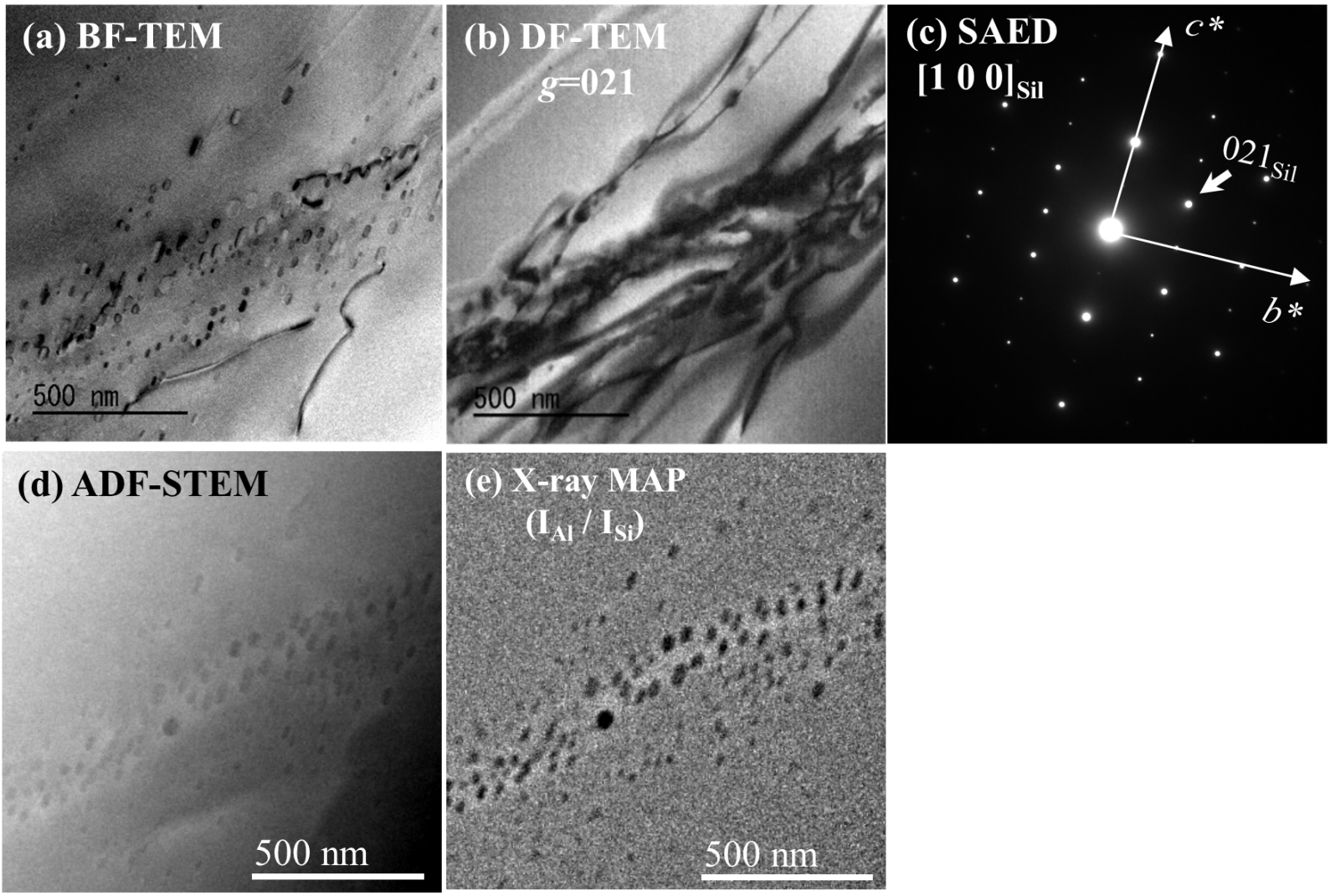
(a) BF-TEM
500 nm
(b) DF-TEM
g=021
500 nm
(c) SAED
[1 0 0]Sil
c*
021Sil
b*
(d) ADF-STEM
500 nm
(e) X-ray MAP
(IAl / ISi)
500 nm

Figure 5

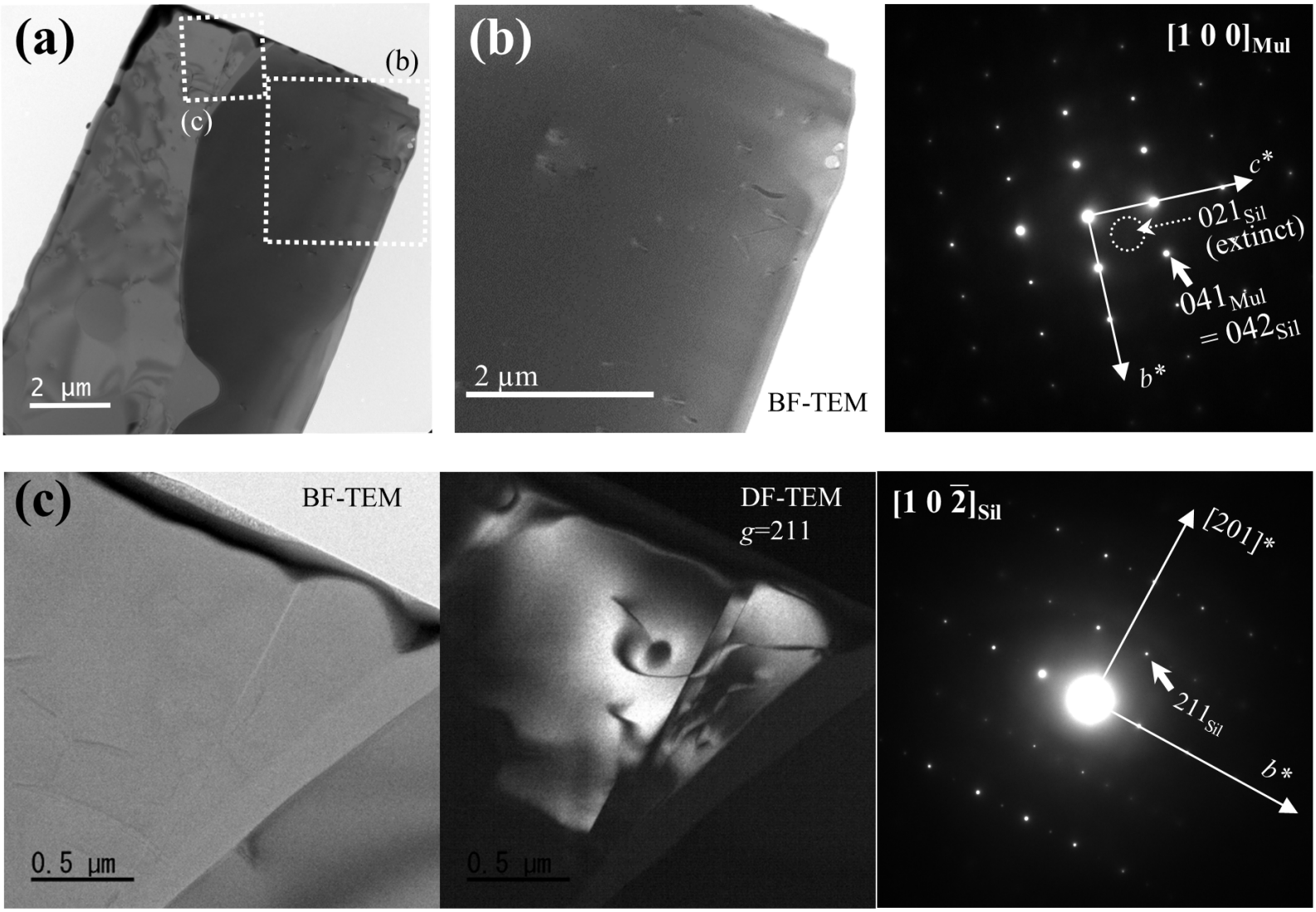
(a)
(b)
(c)
2 μm
(b)
2 μm
BF-TEM
[1 0 0]Mul
c*
021Sil
(extinct)
041Mul
= 042Sil
b*
(c)
BF-TEM
0.5 μm
DF-TEM
g=211
0.5 μm
[1 0 2̄]Sil
[201]*
211Sil
b*

Figure 6

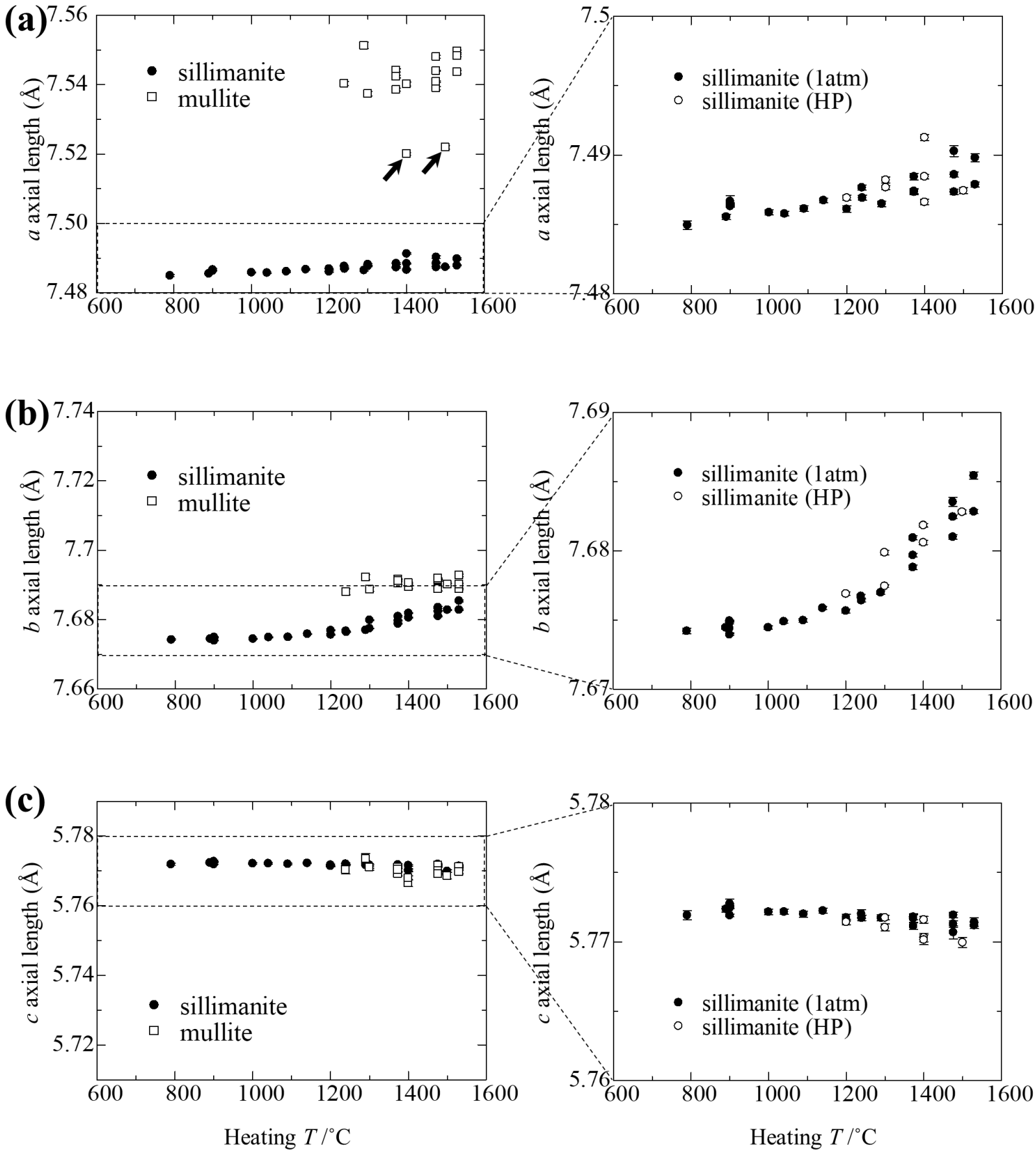
(a)
a axial length (Å)
sillimanite
mullite
sillimanite (1atm)
sillimanite (HP)
(b)
b axial length (Å)
sillimanite
mullite
sillimanite (1atm)
sillimanite (HP)
(c)
c axial length (Å)
sillimanite
mullite
sillimanite (1atm)
sillimanite (HP)
Heating T /°C
Heating T /°C

Figure 7

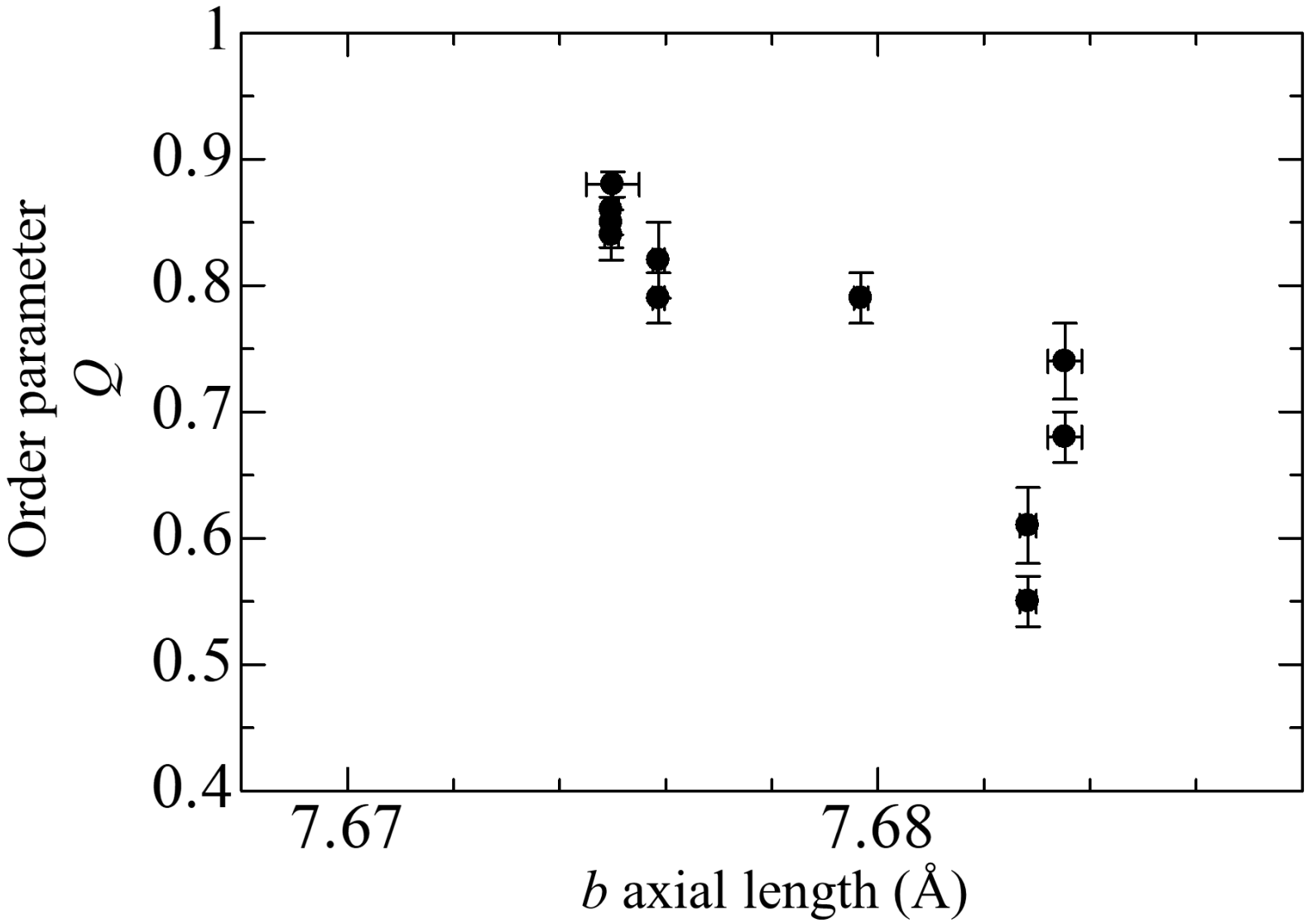

Figure 8

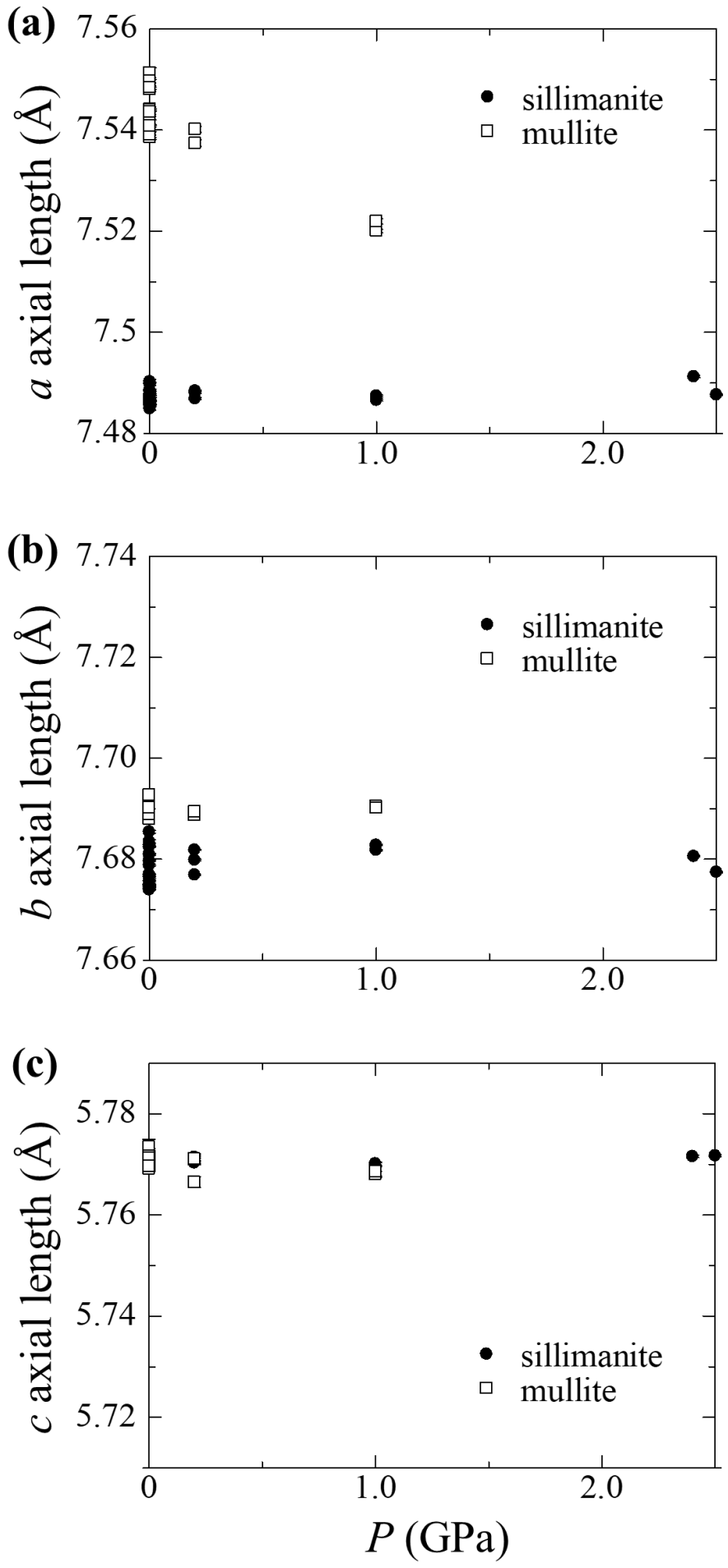
(a)
7.56
7.54
7.52
7.5
7.48
a axial length (Å)
sillimanite
mullite
0
1.0
2.0
(b)
7.74
7.72
7.70
7.68
7.66
b axial length (Å)
sillimanite
mullite
0
1.0
2.0
(c)
5.78
5.76
5.74
5.72
c axial length (Å)
sillimanite
mullite
0
1.0
2.0
P (GPa)

Figure 9

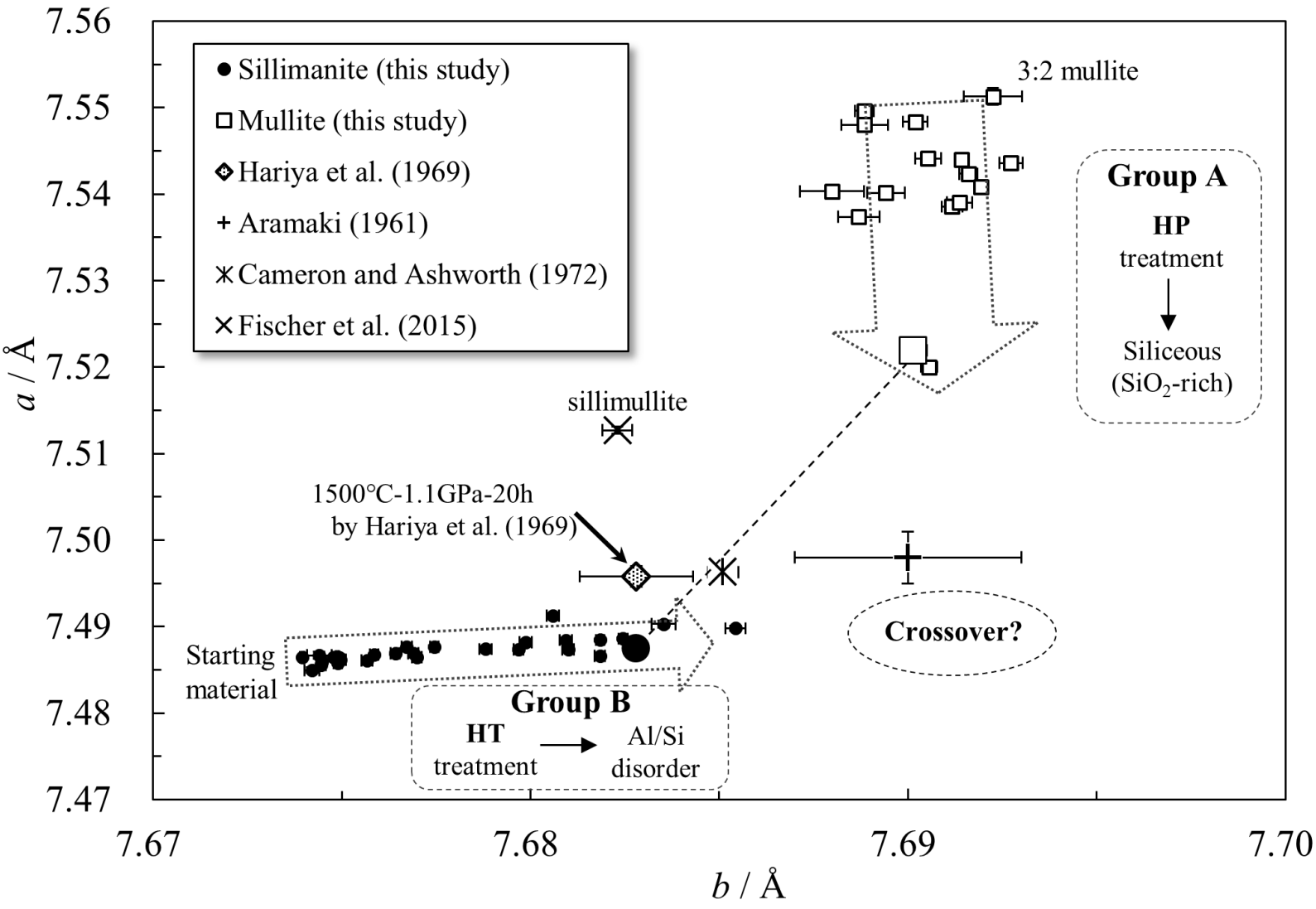
Sillimanite (this study)
Mullite (this study)
Hariya et al. (1969)
Aramaki (1961)
Cameron and Ashworth (1972)
Fischer et al. (2015)
3:2 mullite
Group A
HP
treatment
Siliceous
(SiO_2-rich)
sillimullite
1500°C-1.1GPa-20h
by Hariya et al. (1969)
Crossover?
Starting
material
Group B
HT
treatment
Al/Si
disorder
7.56
7.55
7.54
7.53
7.52
7.51
7.50
7.49
7.48
7.47
a / Å
7.67
7.68
7.69
7.70
b / Å

Figure 10

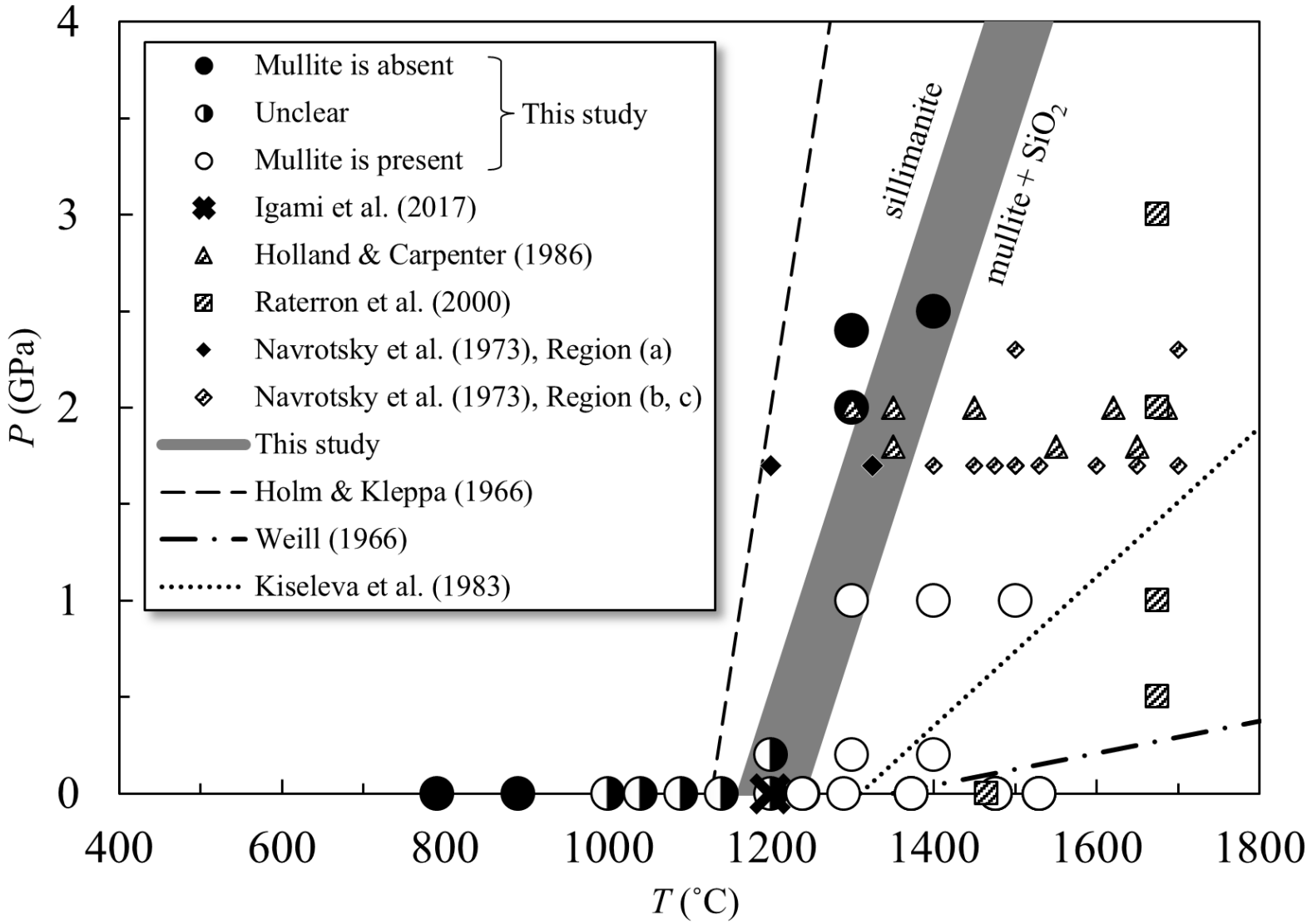
Mullite is absent
Unclear
Mullite is present
This study
Igami et al. (2017)
Holland & Carpenter (1986)
Raterron et al. (2000)
Navrotsky et al. (1973), Region (a)
Navrotsky et al. (1973), Region (b, c)
This study
Holm & Kleppa (1966)
Weill (1966)
Kiseleva et al. (1983)
sillimanite
mullite + SiO2
P (GPa)
T (°C)
0
1
2
3
4
400
600
800
1000
1200
1400
1600
1800

Figure 11

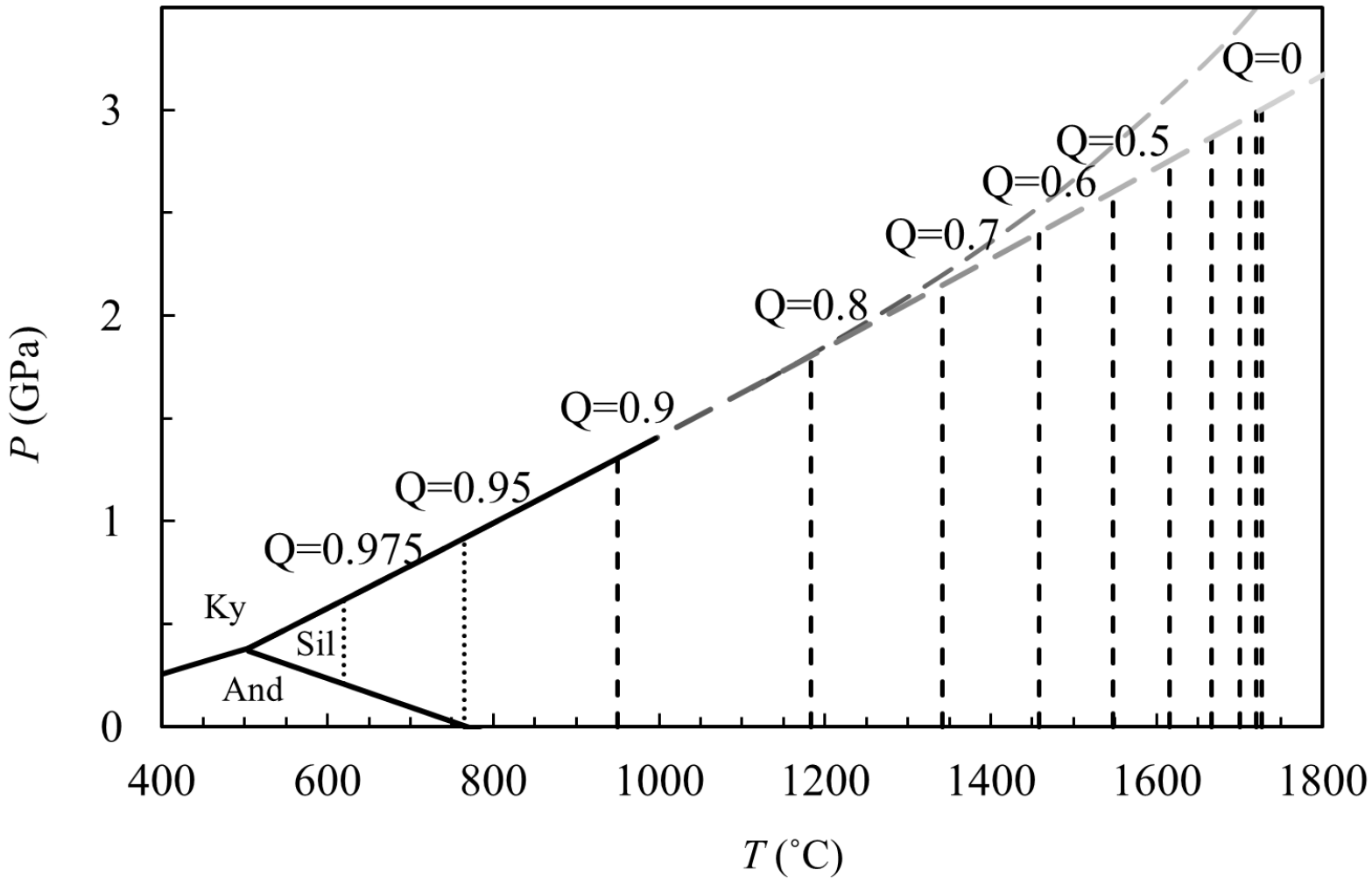
Q=0
Q=0.5
Q=0.6
Q=0.7
Q=0.8
Q=0.9
Q=0.95
Q=0.975
Ky
Sil
And
P (GPa)
T (°C)
0
1
2
3
400
600
800
1000
1200
1400
1600
1800

Figure 12